



Flaw characterization and correlation with cracking strength in Engineered Cementitious Composites (ECC)

Cong Lu^{a,*}, Victor C. Li^b, Christopher K.Y. Leung^c

^a Key Laboratory of Concrete and Prestressed Concrete Structures of Ministry of Education, Southeast University, China

^b University of Michigan, USA

^c The Hong Kong University of Science and Technology, Hong Kong



ARTICLE INFO

Keywords:

Characterization (B)
Pore size distribution (B)
Mechanical properties (C)
Modeling(E)
Engineered cementitious composites

ABSTRACT

Engineered Cementitious Composite (ECC) is a class of fiber reinforced composites showing strain hardening behavior. The variation of cracking strength among various sections of a tensile specimen is a key factor governing the cracking behaviors of ECC. This study employs X-ray computed tomography method to investigate the correlation between cracking strength and flaw distribution in ECC, and identifies the dimensions of pre-existing flaws to be the main influencing parameters. Specifically, the largest cross-sectional area of a flaw perpendicular to stress can be well correlated with cracking strength. To validate the observation, the classic model on first crack strength is modified in this study by adopting a refined fiber bridging relation and employing iterated crack profile. The simulated cracking strength vs flaw size relation is in good agreement with test results. This study provides an improved understanding of the multiple cracking mechanism in ECC, which is useful for material design.

1. Introduction

In view of the quasi-brittle nature of conventional cementitious composites, fibers are incorporated to increase material toughness and to provide ductility. Engineered Cementitious Composite (ECC) is a class of fiber reinforced composites that can reach high tensile strain of several percent while carrying increasing tensile load [1–4]. With the formation of multiple cracks, the crack width in ECC materials can be controlled to under 80 μm [5]. Unlike much wider cracks in conventional concrete, such fine cracks have little effect on the material's resistance to water/chemical transport and they may even exhibit self-healing [6,7]. Compared to concrete members, the durability of ECC members is significantly enhanced [8–10]. With these outstanding properties, various applications of ECC to provide seismic loading carrying capacity, deformability and durability of full scale structures have been proposed and implemented [11–16].

The tensile ductility of ECC have been observed to have higher variability than other properties. High ductility is associated with saturated cracking, where fine cracks at close spacing are formed uniformly along the tensile specimen. However, unsaturated cracking, with clusters of cracks interspaced by un-cracked specimen segments, is commonly observed. This phenomenon is mainly due to the large variation of cracking strength among different parts of the tensile member,

as segments with higher cracking strength may not undergo cracking before ultimate failure occurs in sections with lower strength. The full deformation capacity of ECC may not be realized. The variation in cracking strength can be attributed to: 1) distribution of matrix inherent flaws and 2) variation of fiber reinforcement content [17]. Between the two factors, it is considered by many researchers that the flaw distribution dominates [1,17]. This will also be supported by the modeling results in the present study.

Among the methods to investigate the distribution of flaw size [18,19], prior experimental study [20] examined the flaw size distribution by cutting a tested specimen into a number of sections. As shown in Fig. 1 [20], each section was photographed, after which the images were subjected to thresholding in the Image-J software to distinguish the flaws from matrix. The maximum flaw size at each section was then determined. However, as cutting with a saw causes a loss of several millimeters in specimen thickness, the size of the same flaw measured from the sections on the two sides of the cut is usually different. This generates considerable error in determining the flaw size. Moreover, only a limited number of sections can be practically cut so the section with the largest flaw may not be truly located. The section cutting method is therefore not sufficiently accurate for the quantitative correlation of composite cracking strength to flaw distribution. A better method needs to be introduced.

* Corresponding author.

E-mail addresses: cluab@connect.ust.hk (C. Lu), vcli@umich.edu (V.C. Li), ckleung@ust.hk (C.K.Y. Leung).

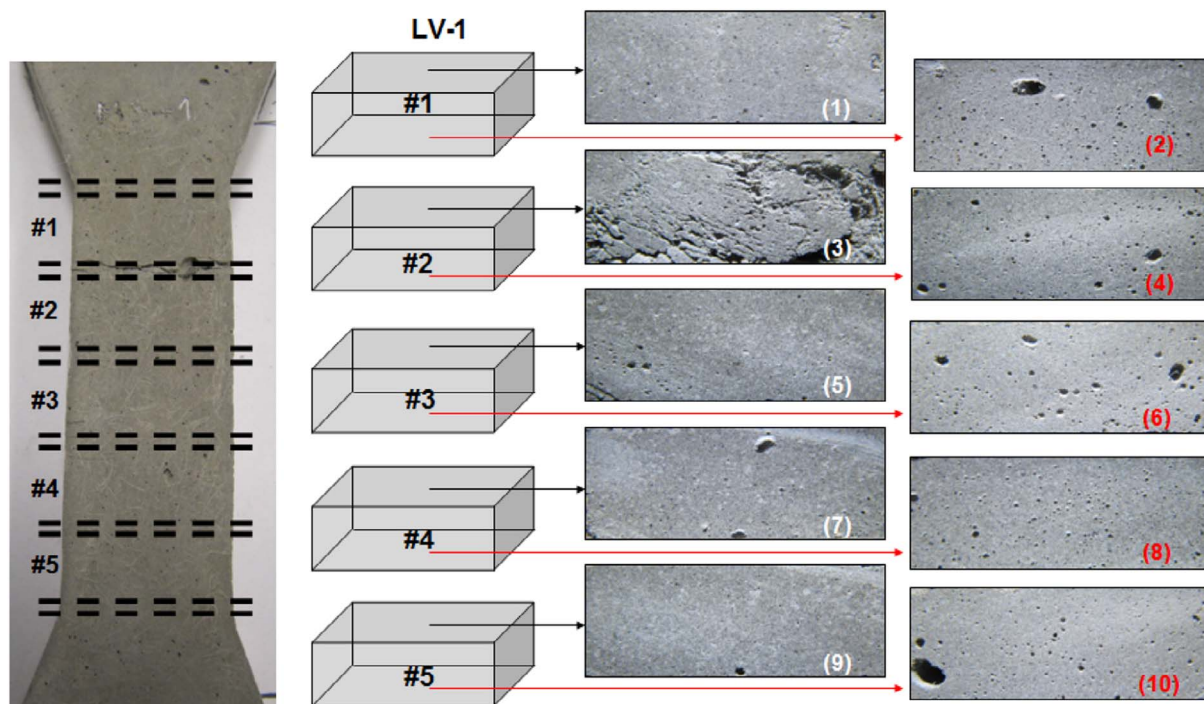


Fig. 1. Sections of a specimen cut and analyzed [20].

X-ray computed tomography (μ CT) is a modern technique most widely used in medical science. It can reconstruct the 3D model of a sample without destroying the original, by collecting 2D projections at different angles around an axis of rotation [21]. When an X-ray beam illuminates and transmits through the sample, the beam intensity will be attenuated after absorption by the different phases and components of the material [6]. Generally, a unit with higher density will absorb more X-ray. The intensity of the transmitted X-ray beam is recorded by a digital detector and the value of the attenuation coefficient for each voxel is transformed into CT numbers according to the Hounsfield scale [22]. After the collection of raw data, a set of gray-scale 2D cross sections that depicts the density distribution within the sample can be constructed. These 2D images can then be used to reconstruct the 3D model of the internal structure. There have been several studies using this technique to map the internal flaw structure or cracking in composites. In [23], X-ray micro-tomography was used to characterize the internal geometry of flaws and micro-cracks in fiber-reinforced polymer laminates. In [6], X-ray computed micro-tomography is adopted to derive three-dimensional morphological data on micro-cracks in ECC before and after self-healing. In this study, this technique will be employed to study the correlation between flaw distribution and cracking strength in ECC composites for the first time.

The present study involves both experimental and theoretical investigations. For the experimental part, with the use of X-ray computed tomography method, the internal structure of the composites will be revealed and the size and shape of flaws are then assessed. Meanwhile, the formation time for each crack will be recorded by taking photos during the tensile test and the cracking strength of them can then be determined by locating the time points in the stress-strain curve. The flaw distribution will then be correlated with the corresponding cracking strength. For the theoretical part, a refined model for ECC cracking strength based on the classic model in [1] will be proposed. Modeling and experimental results will then be compared and discussed.

2. Experimental procedures

2.1. Materials and mix proportions

This study is aimed at evaluating the influence of flaw distribution on the cracking behavior of ECC. Specimen is therefore prepared for uniaxial tensile test. The ECC mixture used for this study was developed by the Advanced Civil Engineering-Materials Research Lab (ACE-MRL), at the University of Michigan. The mix proportion is tabulated in Table 1.

The mixing of the ECC material was conducted according to a standard procedure [24]. The fresh ECC was cast into a dogbone-shaped mould (Fig. 2) which is designed to prevent failure at the ends caused by stress concentration. The specimen was demoulded after 24 h and then cured for 7 days in a curing room with temperature of $23 \pm 2^\circ\text{C}$.

2.2. Testing with simultaneous image recording

The uniaxial tensile test was performed on a Material Testing Machine and the tensile loading was applied at a displacement rate of 0.5 mm/min. During loading, photographs of the specimen surface were taken to capture the formation of cracks. Since the cracks in ECC are very fine, especially at their initiation stage, it is desirable to achieve the highest possible resolution in the captured image. With this objective, a macro lens with magnification of 1:1 was used on a full-frame camera (model: Nikon D610) with the resolution of 6016×4016 . Mounted on a tripod, the camera was placed in front of the MTS machine (Fig. 3). After the focus was placed manually on the sample surface, a remote timer was used to take one photograph every second, so the formation time of each crack can be captured with sufficient precision.

Table 1
Mix proportion for ECC (by weight ratio).

Cement	Fly ash	Sand	Water	Superplasticizer	Fiber
0.3	0.7	0.36	0.25	0.4%	2%

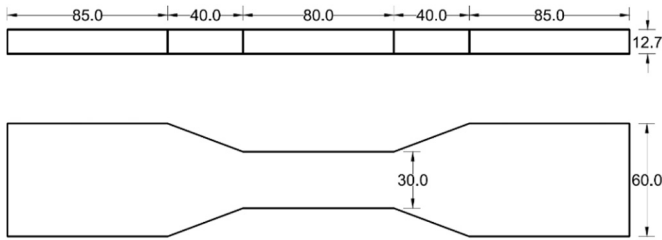


Fig. 2. Dimensions of dogbone shaped specimen for uniaxial tensile test (units:mm).



Fig. 3. Tensile test setup with camera capturing pictures.

2.3. X-ray computed tomography scanning on tested sample

After tensile testing, X-ray computed tomography scanning on the tested specimen was conducted in the SoD mCT Core Lab at University of Michigan. The resolution of the scanning is constant at 2312 pixels by 2349 pixels, so larger sample size will reduce captured details. To restore the small cracks and flaws precisely, very small blocks (30 mm × 12.7 mm × 9 mm) were selected and cut from the tested specimen to be scanned. The blocks were placed in a 16 mm diameter specimen holder and scanned over their entire length using a micro-CT system shown in Fig. 4 (μ CT100 Scanco Medical, Bassersdorf, Switzerland). Scan settings were set as: voxel size 6.6 μ m, 0.1 mm CU filter, and integration time 500 ms.

After the scanning, several thousands of μ CT images were acquired and one of them is shown in Fig. 5 as an example. The image shows a slice of 2D gray-scale cross-section where de-noising and segregation needs to be performed before the cracks and flaws can be distinguished from the background. Details on the image analysis will be described in the next section.

3. Processing of imported μ CT images

To separate the flaws and cracks from the matrix, processing was conducted on the acquired μ CT images. The images are basically composed of two phases: (1) gas phase including flaws and cracks, which appears black and (2) solid phase including the matrix (cementitious binder and fine aggregates) and fibers, which appears as lighter gray. With the color difference, thresholding on the gray scale intensity can be performed to identify the flaws. When performing the image processing, two different scenarios need to be considered for selecting the proper processing method:

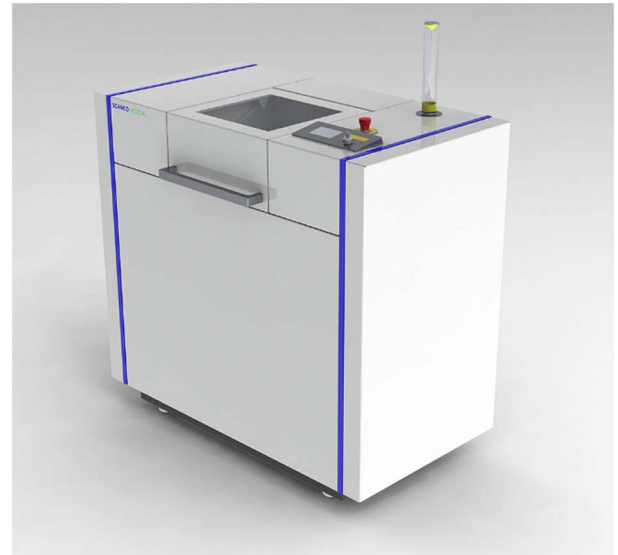


Fig. 4. Micro-CT system in SoD mCT Core Lab, University of Michigan.

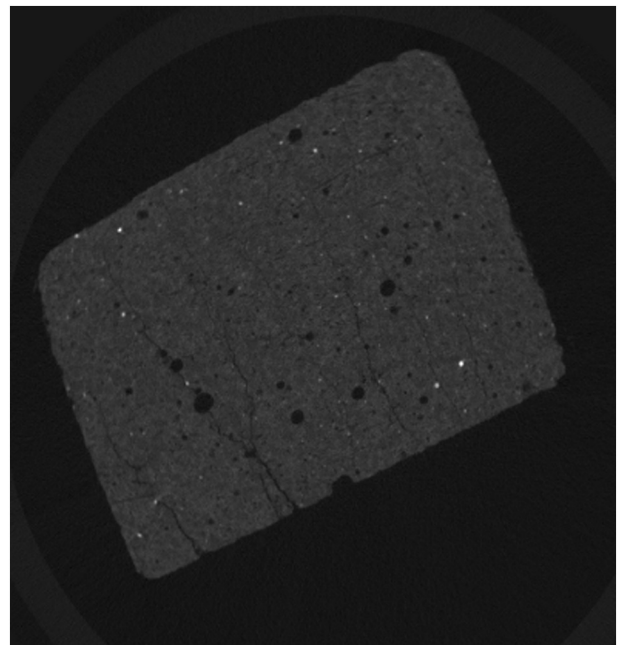


Fig. 5. An example of imported μ CT image.

- 1) if the processing objective is to have an overall view of crack/ flaw distribution as well as how cracks and flaws intersect with each other, both cracks and flaws need to be preserved whereas other noises should be eliminated.
- 2) if the distribution of flaws size and shape is to be determined, only flaws need to be preserved whereas both the cracks and noises should be removed.

In the first scenario, the gray-scale images are first converted into binary images based on a properly set threshold value which turns on darker pixels to highlight the air phase and turns off the others that represent solid phase. The binary images are then stacked into a matrix of voxels. The gas phase in the matrix is partitioned into different connected components, also called clusters, by means of voxel connectivity. Voxel connectivity defines the way voxels are connected to their neighbors. In current case, the connectivity is set as 6-connected neighborhood in three dimensions, which means only voxels sharing

one of their top, bottom, left, right, front and rear surfaces are considered as connected. Other connectivities like 18-connected (where voxels sharing edges are regarded as connected) or 26-connected (where voxels sharing vertices are regarded as connected) neighborhood may lead to the overestimation of voxel number in the cluster. In this study, to reduce the computational effort, the small capillary flaws were first removed by setting a minimal volume filter to the clusters to preserve only larger flaws and crack. Subsequently, based on the 2D and 3D geometry-topology characteristics obtained from the clusters' matrix, main cracks can be distinguished by their large size in the transverse dimension (the direction along which the cracks propagate) and main flaws can be distinguished by their large volume. Segregation of cracks and flaws can then be realized. Further details of the process can be found in [6].

In the second scenario, only the inherent flaws need to be identified. As the cracks which interact intensively with flaws will make it difficult for the flaw structure to be clearly revealed, they should be eliminated. A median filter was therefore applied to perform image blurring where the grayscale of pixels on cracks will be influenced and neutralized by the surrounding grayscale, so the cracks do not show up as dark as the large flaws. Thresholding methods was then applied in a way to retain the large flaws alone. After this step, another thresholding on flaw size was applied to preserve flaws with nominal radius larger than a set value, so the flaws of interest can be identified (Note: nominal radius is calculated from the flaw volume assuming the flaws are spherical).

4. Experimental results and discussions

The correlation between flaw distribution and composite cracking strength can be affected by many factors. For example, even for specimens in the same batch, the fiber content and matrix toughness may vary. Also, alignment in the testing setup is not always perfect for all the specimens. These factors can affect the cracking behavior of ECC and therefore bring more variables into the correlation. To reduce the effects of various factors, only one specimen is studied and analyzed in this initial study. In the future, more tests can be performed to obtain a better understanding of the different effects. Because data is collected at many locations on a given specimen, a single tensile test should still yield useful insights on the correlation between flaw distribution and the composite cracking strengths.

In Fig. 6, the applied stress is plotted against the test time. The typical multiple cracking behavior of ECC can be observed from the stress jumps in the curve after about 100 s. The test was terminated at time of 325 s to avoid final failure, so the images of the internal crack/flaw

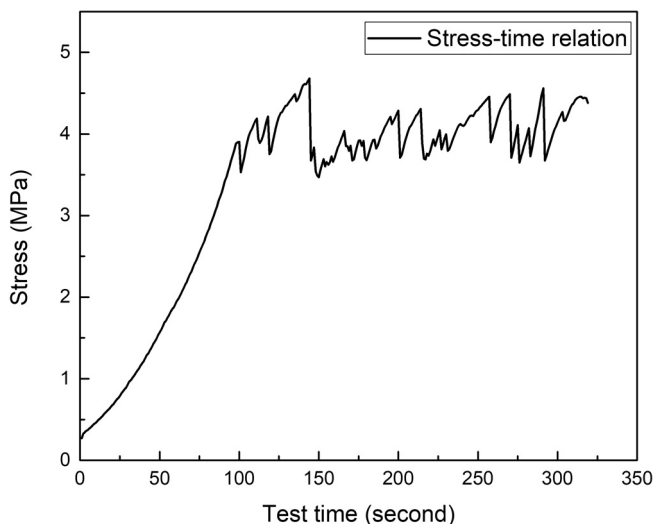


Fig. 6. Relation of stress versus test time.

structures will not be masked by the localized crack which can be very large. Since this study is aimed at studying the mechanism of cracking strength in ECC, the actual strain capacity is not of interest and therefore not measured in the test. In the following sub-sections, the results from μ CT scanning will be investigated to reveal the correlation between flaw distribution and cracking strength in the ECC.

4.1. Comparison between regions with/without cracks

The cracking patterns of the tested specimen are shown in the left hand side of Fig. 7. As mentioned before, small blocks were taken from two representative regions of the specimen as indicated by the red boxes. One region (region A) shows saturated multiple cracking while no crack is observed in the other region (region B). The 3D reconstructed renderings of the two regions are shown on the right hand side of Fig. 7.

The gas phase in both regions were rendered to reveal the flaw structure. To be specific, in region A, the cracks were deleted by the approach described in the second scenario of image processing section, after which a thresholding on flaw size was applied to reserve large flaws with nominal radius larger than 0.2 mm. The 3D renderings of large flaws in both region A and B after processing are shown in Fig. 8 a and b respectively.

From Fig. 8, both the 3D reconstructions of flaw structures in regions A and B reveal a considerable number of flaws with 0.2 mm nominal radius or larger, but the largest flaws are found in region A. The flaw size distributions in region A and B are statistically shown in Fig. 9, where the number of flaws per cubic centimeter in each size range is plotted against nominal radius. Given the fact that none of the flaws develops into a crack in region B, it is surprising that region B outnumbers region A in flaws with radius range of 0.2–0.4 mm. In the radius range of 0.4–0.7 mm, both regions present similar flaw populations, but region A contains two large flaws within 0.7–1.1 mm while region B does not. Considering the significant difference of cracking behavior between the two regions, this result suggests that cracking is likely to be induced by the largest flaw while the population of smaller cracks has less influence.

4.2. Comparison of cracking bands in region A

A more detailed analysis is conducted within the cracking region A. Saturated cracking was observed in region A, and the pattern is complicated by the fact that some of the cracks are connected together. As the μ CT images can only be taken after the test was finished, it is not possible to backtrack how the cracks are developed inside the specimen and joined together during the test. Instead of trying to identify individual cracks from connected ones, this study focuses on 'cracking bands', which is defined as a group of individual cracks connected with each other. When identifying these bands, visual inspection of the μ CT images is necessary to make sure that no connection exists between cracks from different bands. The initiation of each band is then ensured to be independent from other bands. With the photographs of specimen surface taken during the test, the time when each band is first initiated can be determined. The corresponding first crack strength (i.e. the stress when cracking first occurs) of each band can then be obtained from the test data at that time and correlated with the internal flaw structure captured by μ CT images.

After examining the connectiveness of internal cracks from μ CT scan images, region A can be divided into three cracking bands as shown in Fig. 10a, denoted as band A-1, A-2 and A-3 respectively. The internal gas phase is rendered in Fig. 10b. It should be noted that some of the cracks are very tight and difficult to be distinguished from the background by automatic segmentation. As a result, they do not appear on the rendering in Fig. 10b. This rendering is only a graphical demonstration of the main cracks/flaw structure. It can be expected that a more complete 3D rendering including the extremely tight cracks can

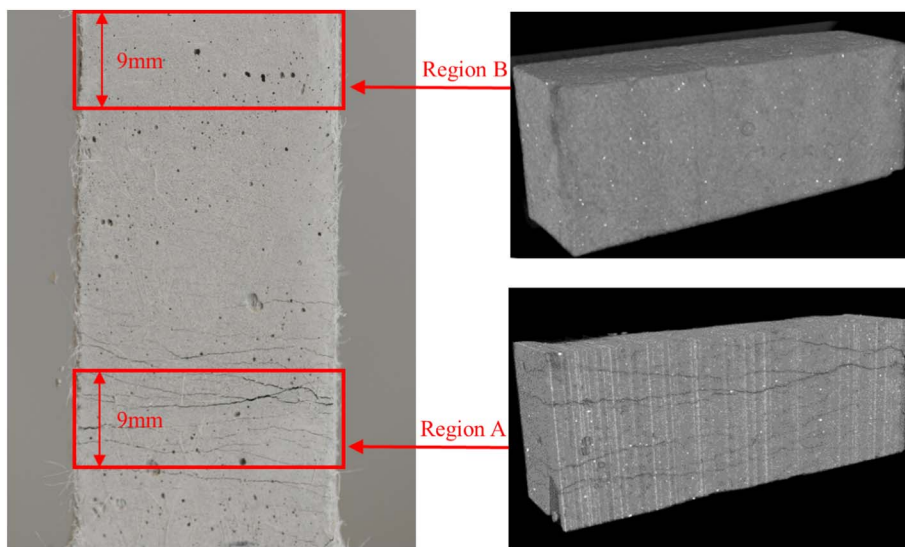


Fig. 7. Schematic diagram for two regions cut out from original specimen.

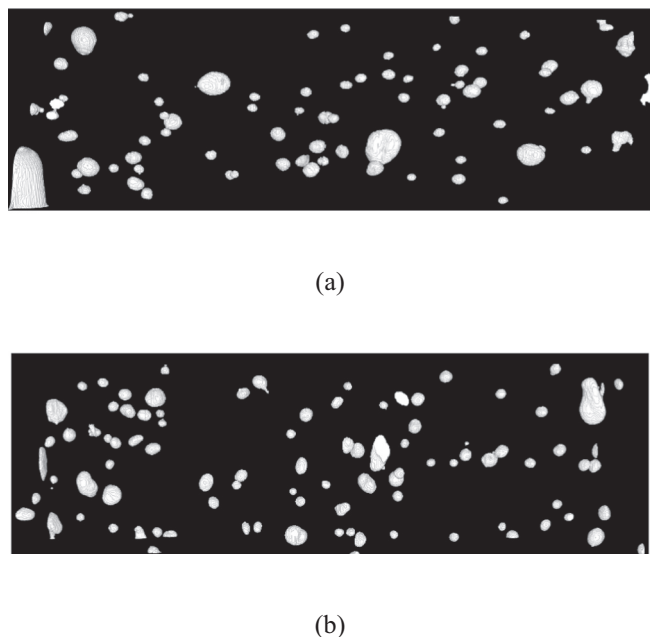


Fig. 8. The rendered 3D reconstruction of large flaws in a) Region A, and b) Region B.

be achieved with higher resolution μ CT scan equipment.

After dividing the multiple cracks of region A into three bands, the initiation of each band can be tracked. Taking band A-1 for instance, from the photographs taken during the test, it is found that cracking in band A-1 is first observed at the photograph taken at 145 s after the start of the test. From the stress-time curve, it can be seen that the applied stress just dropped from a peak of 4.679 MPa at 145 s (Fig. 11). This indicates the first crack strength of band A-1 is 4.68 MPa. In a similar manner, the first crack strength (cracking strength) is found to be 4.56 MPa for band A-2 and 4.07 MPa for band A-3, as shown in Fig. 11.

For the three cracking bands, the patterns when the first crack was observed and when the test was terminated are shown in Fig. 12. In addition, The 3D rendering of the internal flaws with nominal radius larger than 0.2 mm for all bands are also shown. The column graph listing the flaw number per cubic centimeter within different nominal radius range is plotted in Fig. 13 for the three bands. In the radius range of 0.2–0.3 mm, the flaws in A-1 and A-2 slightly outnumber A-3, while

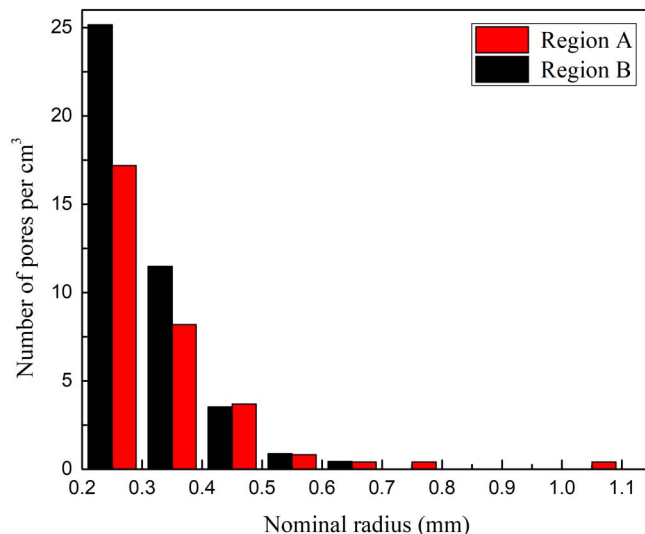


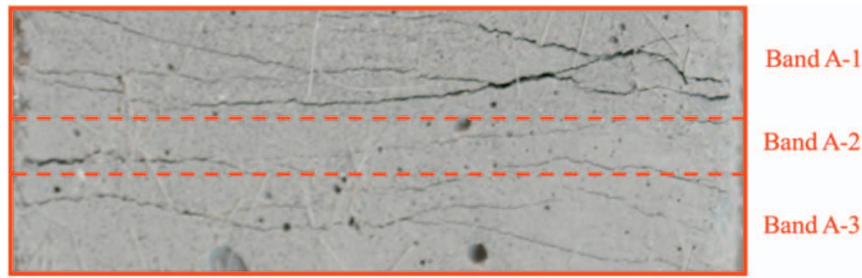
Fig. 9. Distribution of flaw size in region A and B.

A-3 has more flaws with radius ranging from 0.3 to 0.4 mm. Also, the maximum flaw size in band A-3 (1.0–1.1 mm) is significantly larger than those in A-1 (0.6–0.7 mm) and A-2 (0.7–0.8 mm). Consequently the first crack strength of A-3 (4.07 MPa) is smaller than A-1 (4.679 MPa) and A-2 (4.56 MPa). This result indicates again that the first crack strength is more strongly correlated with the largest flaw size rather than the number of smaller flaws.

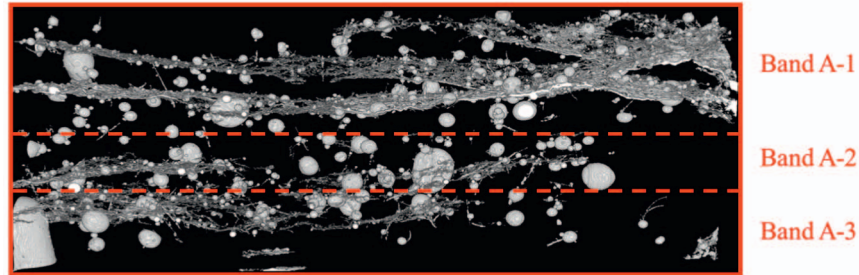
4.3. Further discussion

When comparing the flaw distribution in Band A-1 and region B, it is interesting to see that the largest flaw size is similar in both regions, and region B even has a larger number of smaller flaws (0.2–0.5 mm), as shown in Fig. 14. This seems to be contradicting with the fact that band A-1 cracked at 4.679 MPa, while no crack occurred in region B. This observation implies that the largest nominal flaw size and the number of flaws cannot be used as the only factors to explain the difference in cracking behaviors but that the shape of the flaws needs to be taken into consideration.

Fig. 15 shows the three largest flaws in band A-1 (Fig. 15a) and region B (Fig. 15b), where the direction of tensile loading is marked by



(a)



(b)

Fig. 10. a) Dividing region A into three cracking bands, b) 3D rendering of inside gas phase of the three bands.

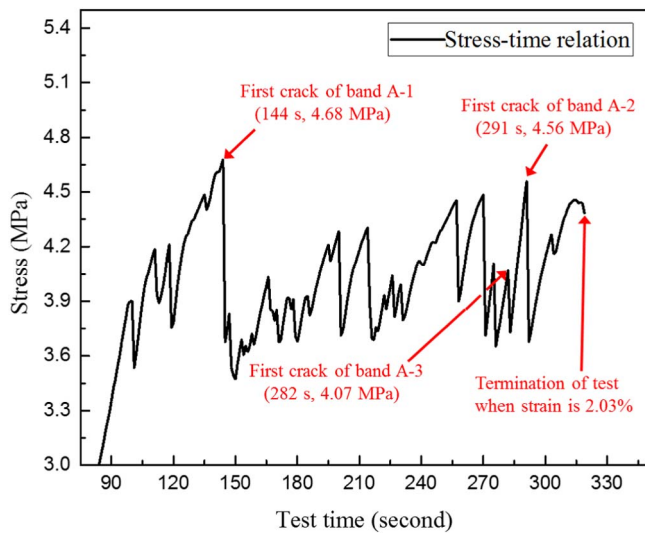


Fig. 11. Time point and stress when each band first cracked.

arrows. It is shown that flaws in band A-1 are shaped like spheres, while those in Region B are shaped more like ellipsoids of which the major axis is roughly parallel to the loading direction. Consequently, in comparison with region B, the flaws in band A-1 have a larger cross-section perpendicular to the loading direction and also higher stress concentration around the flaw.

To have an overall comparison of the flaw shapes in band A-1, A-2, A-3 and region B, the largest cross-section in each flaw that is perpendicular to the loading is determined and plotted in Fig. 16. From the figure, band A-3 has flaws with much larger perpendicular-to-loading cross-section. Given the fact that band A-3 also has the largest flaw in terms of volume it is reasonable that it exhibits lower first cracking strength than band A-1, A-2 and region B. Then from the comparison of

band A-1, A-2 and region B, the plot shows that the flaws in band A-1 and A-2 have larger perpendicular-to-loading cross section, ranging from 0.8 mm² to 1.2 mm². As a result, although the largest flaw size in band A-1 (in terms of nominal radius) is similar as region B, the larger section area perpendicular to loading makes it easier to initiate a crack. In fact, the cracking strength of band A-1 (4.679 MPa) is the highest stress applied in the test as the test was terminated before reaching ultimate failure. If the test was not stopped until failure, region B might crack at a stress higher than 4.679 MPa.

The previous discussions indicate that the largest dimensions of flaws play a more important role in determining the cracking strength of ECC, rather than the population of flaws. The cracking strength of band A-1, A-2, A-3 and region B is therefore plotted in Fig. 17 against the largest perpendicular-to-loading cross-section area for each of them. As region B did not crack before the test was terminated, we assume it to have a cracking strength of 4.9 MPa to fit the trend in the graph. As can be concluded from Fig. 17, the overall correlation (despite the middle points which show a slightly reverse trend) is reasonable, where the first cracking strength decreases continuously with increasing flaw section area. In other words, flaws with larger section area perpendicular to loading are considered to be more prone to cracking.

The above observation is in agreement with fracture mechanics principles. In the following section, theoretical modeling of the first crack strength of ECC will be carried out as a comparison with above observations.

5. Modeling first crack strength of composites with various flaw sizes

To validate the observed correlation between first crack strength of fiber composites and flaw dimensions, theoretical modeling needs to be conducted. This section will first briefly review an existing model on first crack strength in fiber composites, which was simplified by several assumptions. A modified model is then proposed which adopts a more refined fiber bridging relation and iterated crack profile. Lastly the

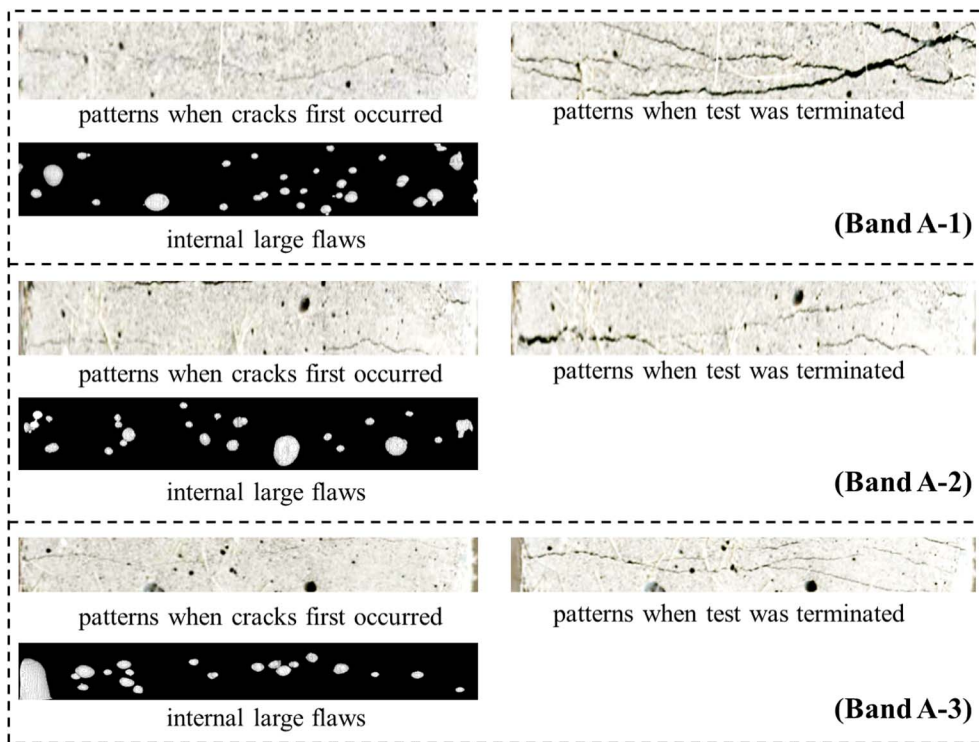


Fig. 12. Patterns when cracks first occurred, patterns when test was terminated and internal large flaws for band A-1, A-2 and A-3.

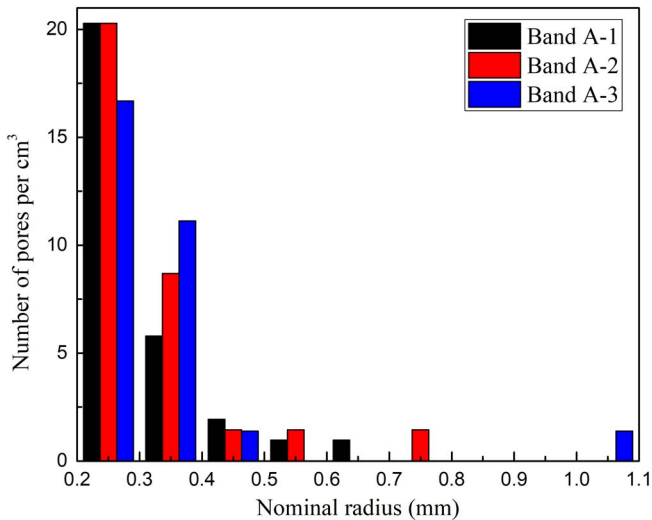


Fig. 13. Distribution of flaw size in band A-1, A-2 and A-3.

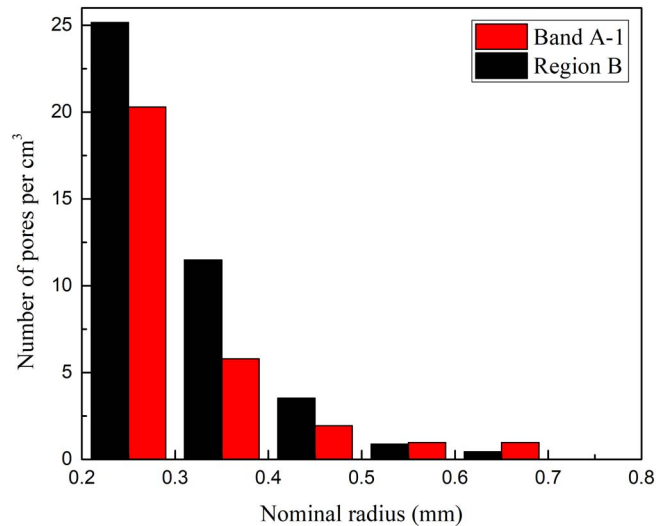


Fig. 14. Distribution of flaw size in band A-1 and region B.

comparison between the simulation results and μ CT scanning results is presented.

5.1. Existing model on first crack strength

The relation between first crack strength and inherent flaw size in ECC has been one of the fundamental topics that provides the theoretical basis for multiple cracking in fiber reinforced composites [1]. For the case of aligned continuous fiber reinforced composites, the cracking strength has been discussed for different modes [25], i.e., short cracks with cracking strength dependent on flaw size and long cracks that have reached a steady-state propagation [26]. The work in [27] extended the discussion to a random short fiber case, where the flaw (since a flaw can be regarded as an initial crack, flaw size is mentioned as ‘crack size’ in the following discussions following convention) is assumed to be of

penny shape and fully bridged by fibers in an infinite body under uniform tension. A schematic 2-D diagram is shown in Fig. 18, with the radius of the penny denoted as c . The first crack strength is calculated as the applied tension at which the totaled stress intensity factor at the crack tip due to the applied stress σ_a and fiber bridging stress σ_b equals the critical composite toughness K_{tip} .

To obtain the crack tip stress intensity due to fiber bridging, the crack profile (crack opening at any position along the crack) needs to be derived. For a penny-shaped crack, the stress intensity factor at the crack tip is calculated as:

$$K_L = 2(c/\pi)^{0.5} \int_0^1 \frac{[\sigma_a - \sigma_b(X)]XdX}{\sqrt{1-X^2}} \tag{1}$$

where $X = x/c$, and x denotes the distance of a point from the middle of the crack. The crack opening can be computed with the stress

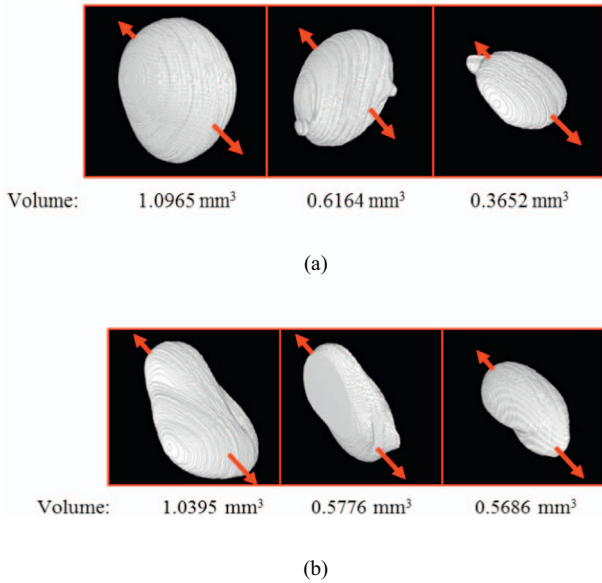


Fig. 15. Top three largest flaws in a) Band A-1, and b) Region B.

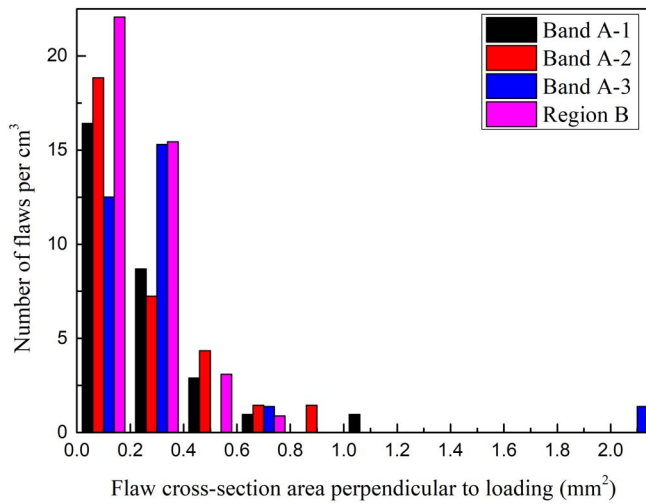


Fig. 16. Distribution of largest perpendicular-to-loading cross-section area in each flaw.

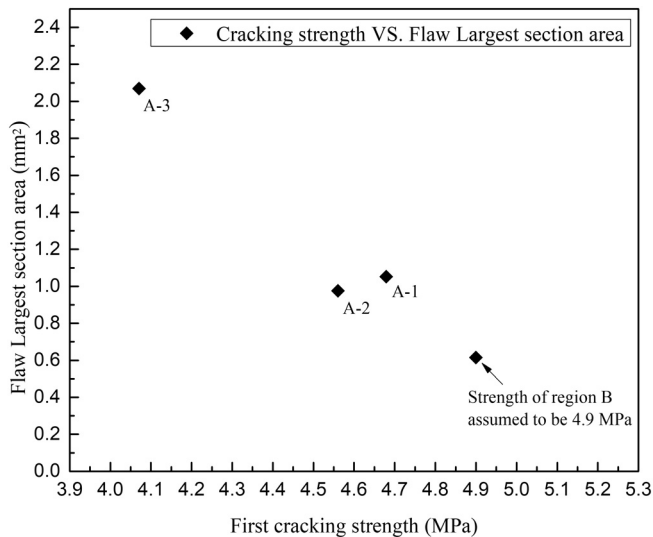


Fig. 17. Correlation between first crack strength and flaw largest cross-sectional area perpendicular to loading.

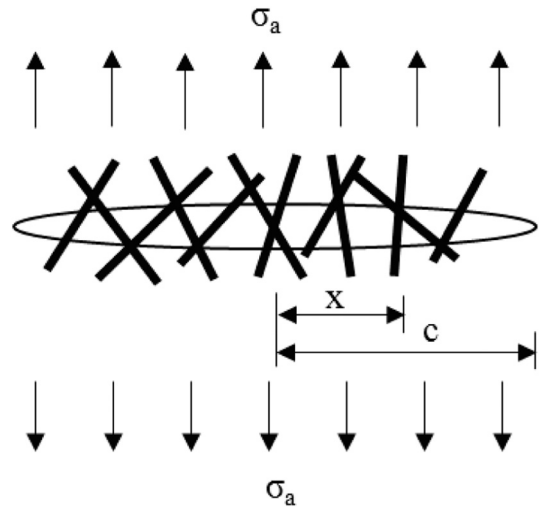


Fig. 18. A penny-shaped flaw bridged by short random fibers.

distribution as [25]:

$$\delta(X) = \frac{8(1 - \nu^2)c}{\pi E_c} \int_X^1 \frac{1}{\sqrt{s^2 - X^2}} \times \int_0^s \frac{[\sigma_a - \sigma_b(t)]tdt}{\sqrt{s^2 - t^2}} ds \quad (2)$$

where ν is the Poisson's ratio for the matrix and E_c is the elastic modulus of the composites, which is taken as $E_m V_m + E_f V_f$. E_m , E_f and V_m , V_f stand for the elastic modulus and volume fraction for matrix and fibers respectively. In [27], an approximate crack profile is obtained by assuming uniformly distributed stress along the crack flank and adjusting the magnitude of the stress to give a stress intensity factor equal to the crack tip toughness K_{tip} . Then $\delta(x)$ is obtained by combining Eq. (1) and (2) and setting $K_L = K_{tip}$:

$$\delta(x) = \left(\frac{4(1 - \nu^2)K_{tip}c^{0.5}}{E_c \pi^{0.5}} \right) \left(1 - \frac{x^2}{c^2} \right)^{0.5} \quad (3)$$

With the estimated crack profile in Eq. (3), the stress intensity factor at crack tip can be calculated with Eq. (1) and the first crack strength is then determined.

5.2. Updated bridging stress-crack opening relation

In the calculation of the stress-crack opening relation in previous work [27], the fiber/matrix interface is assumed to be governed by friction alone and chemical bond is neglected. In addition, fiber rupture and slip hardening which are reported to play an important role in fiber bridging behavior [28–30] are also ignored. In this sub-section, an updated bridging stress-crack opening relation adopted from [30] which considers the above factors is used to refine the modeling of first crack strength.

To be more detailed, when the crack opening is small, the chemical bond is significant relative to frictional bond in controlling the debonding process and in contributing to the fiber bridging stress on the crack face. It is therefore included in the present model. During the pullout stage, slip-hardening behavior can be observed where the frictional bond strength can be taken to vary linearly with the slip distance. This effect is also included. The overall bridging relation is obtained by numerically summing up the contributions of every single fiber. During the summation, it needs to be noted that fibers will rupture if they are loaded beyond their apparent fiber strength. These ruptured fibers are then discounted. In addition, since the pullout load of the short side of the fiber can be higher than the long side of the fiber due to slip hardening behavior, the possibility for a two-way pullout is considered as well. Details for the computation of updated bridging relation can be found in [30].

Table 2
A typical set of material parameters.

Fiber	Fiber volume fraction	2%
	Fiber length l_f (mm)	12
	Fiber diameter d_f (mm)	0.039
	Fiber elastic modulus E_f (GPa)	22
	Nominal fiber strength $\sigma_n f_u$ (MPa)	1060
Matrix	Elastic modulus E_m (GPa)	20
	Fracture toughness K_{tip} (MPa m ^{0.5})	0.09
	Poisson's ratio ν	0.2
Interface	Frictional bond τ_o (MPa)	1.31
	Debonding fracture strength G_d (J/m ²)	1.08
	Snubbing coefficient f	0.2
	Fiber strength reduction factor f'	0.33
	Slip hardening parameter β	0.58

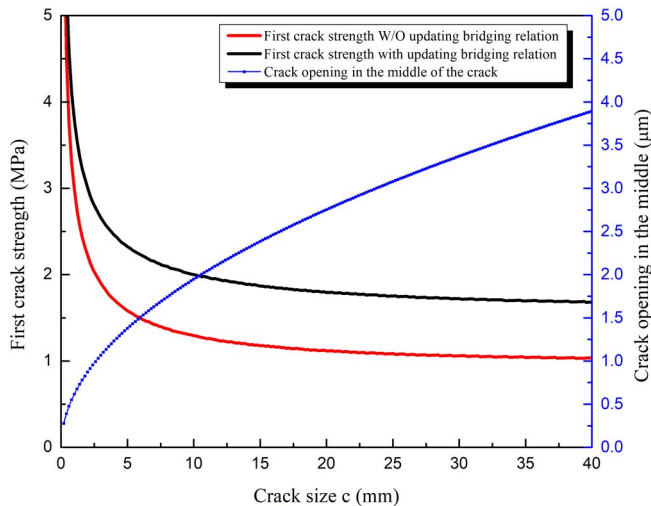


Fig. 19. First crack strength with original and updated bridging relation and approximate crack opening in the middle of the penny-shaped crack for different crack sizes.

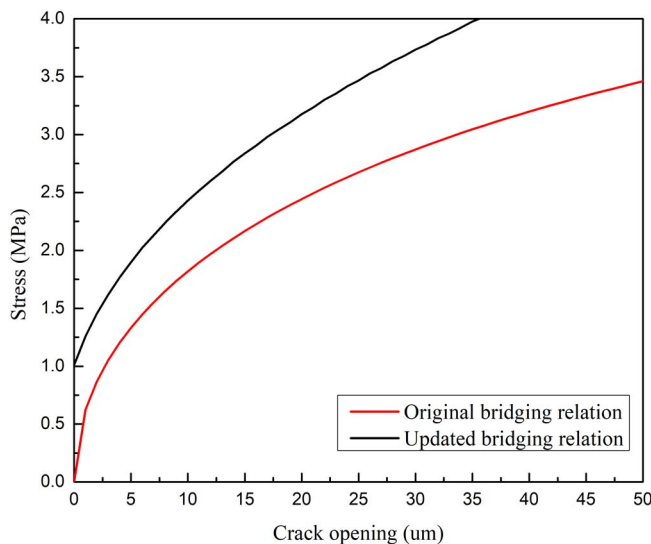


Fig. 20. Original and updated fiber bridging relation.

To demonstrate how the first crack strength is changed when the updated cracking bridging relation is employed, simulation is carried out with a typical set of material parameters from the literature as listed in Table 2 [30,31]. It should be noted that the matrix fracture toughness K_{tip} is taken as 0.09 MPa m^{0.5} which is smaller than that in the literature [26,30]. This is by the consideration that the tensile samples used for μ CT scan had only been cured for 7 days before testing. Fig. 19 shows

the variation of first crack strength with flaw sizes based on both the original [27] and updated stress-crack opening relations. The approximate crack opening in the middle of the crack is also plotted against crack size (Note: as the crack profile is calculated from Eq. (3), the crack opening is independent of bridging relation). The first crack strength is found to be significantly increased by considering the various factors discussed above, among which chemical bond is most influential. As shown in Fig. 19, the crack opening at the middle of the crack is barely 4 μ m when crack size c is as large as 40 mm. At such a small crack opening, the chemical bond is playing a more dominant role in the bridging stress than the frictional bond, as illustrated in Fig. 20 which shows the difference between original and updated bridging relations.

5.3. Results with iterated crack profile

As mentioned above, the crack profile was approximated by assuming a uniformly distributed stress along the crack flank. The numerical analysis in [25] shows that the approximate analytic solution and the exact solution by numerical method converge at small crack sizes, but at large crack sizes the assumption leads to a 20% over-estimation of the first crack strength in aligned continuous fiber reinforced composites. However, this error has not been assessed for short random fiber reinforced composites. In this section, the accurate crack profile and bridging stress distribution are obtained through an iterative process. The crack profile is first assumed to follow Eq. (3) and the bridging stress along the crack flank can then be calculated using the bridging stress-crack opening relation. The bridging stress distribution along the crack is then substituted into Eq. (2) to obtain an updated crack profile. In the next step, the bridging stress is re-calculated with the updated crack profile and used to further update the crack profile until self-consistency is achieved. The first crack strength calculated with estimated and iterated crack profiles are shown in Fig. 21 where very little difference can be found at small crack size c . This is due to the fact that when the crack size is small, the crack opening is also small. The frictional bond transfer is then small so the bridging stress is governed by the constant chemical bond. As a result, the assumption of uniform bridging stress results in a very small error.

The comparison between approximate profile and iterated profile is shown in Fig. 22 for $c = 1$ mm, 5 mm, 20 mm, and 50 mm respectively. A trend similar with the comparison of first crack strength can be found: The approximate profile assuming uniform bridging stress stays close to the iterated profile at small crack sizes ($c = 1$ mm, 5 mm), as the bridging stress is mainly contributed by the constant chemical bond at

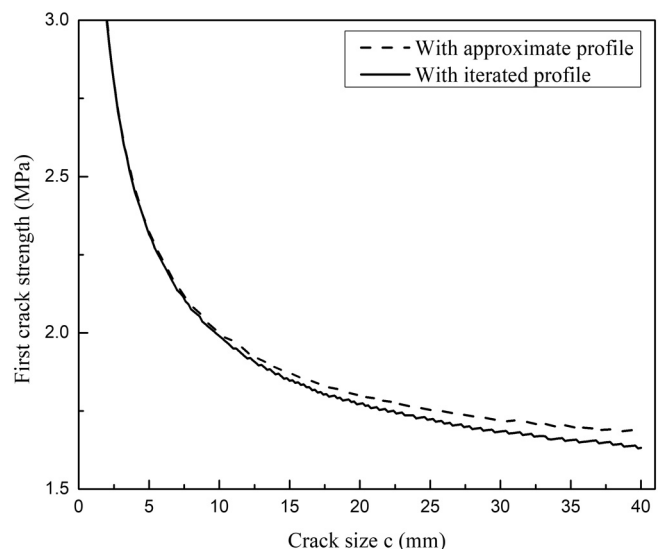


Fig. 21. First crack strength with approximate and iterated crack profile.

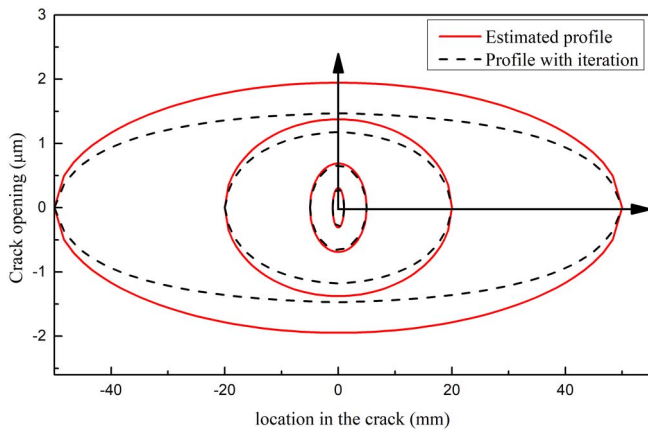


Fig. 22. Approximate and iterated crack profile for various crack size.

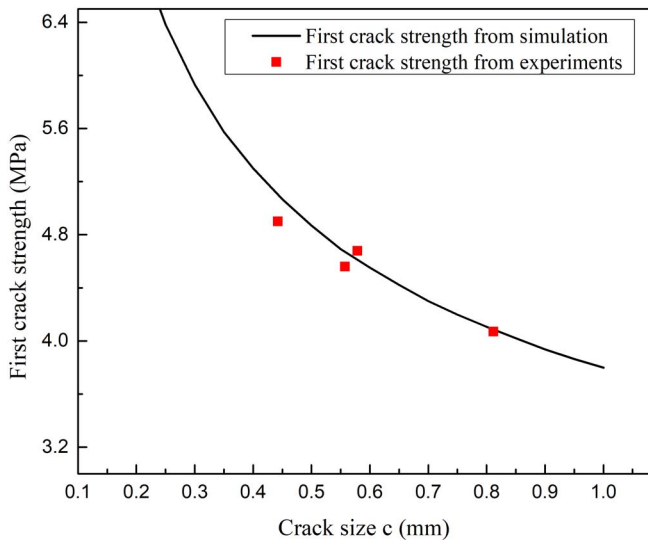


Fig. 23. Comparison between first crack strengths from experiments and simulation.

small crack opening. With increasing crack size c , the difference also increases.

To compare with the experimental observation in Fig. 17. Both the first crack strengths from simulation and experiments are plotted in Fig. 23. Specifically, the crack size c for the experimental first crack strength is translated from the largest cross-sectional area perpendicular to stress, by assuming this cross-section are in circular shape with radius c .

As can be seen from the figure, with the use of reasonable micro-mechanical parameters, the simulation can capture a clear trend which agrees with the experimental results very well. Note that the inherent flaws observed from μ CT images are mostly three dimensional and not bridged by fibers since the fibers tend to be embedded in the paste rather than in air bubbles during material casting. Given the fact that the modeling takes the assumption of penny shape crack which may not be the case in reality, the simulation results are still able to reveal the decreasing trend of first crack strength with increasing flaw dimensions.

6. Concluding remarks

The variation of cracking strength in ECC composites is considered to be a governing factor for their multiple cracking behavior. This study investigates the correlation between the cracking strength and the inherent flaws by X-ray computed tomography method. The results imply that the flaw size (to be specific, the flaw's largest section area perpendicular to loading) is a key parameter that correlates well with

matrix cracking strength. It needs to be pointed out that due to the limited size of μ CT scan samples, the tedious computation to process μ CT data and the complicated patterns of micro-cracks in ECC, only limited results can be exacted from experiments at this stage. A further study with more advanced facilities and optimized algorithm would be helpful in the future to better support the argument.

The theory on first crack strength in ECC composites is also modified in this study by considering more factors in the crack bridging stress vs opening relation and employing iterated crack profile. The new model reveals how the first crack strength is dependent on the flaw dimension, which agrees well with the tests. Through this study, a more comprehensive understanding on the cracking mechanism can be achieved, which can facilitate the micromechanics-based material design of ECC.

Acknowledgement

The authors would like to thank the SoD μ CT Core Lab in University of Michigan for providing the X-ray computed tomography facilities. Also, financial support of this work by the Hong Kong Research Grant Council through GRF 16205414 is gratefully acknowledged.

References

- [1] V.C. Li, C.K.Y. Leung, Steady-state and multiple cracking of short random fiber composites, *J. Eng. Mech.* 118 (1992) 2246–2264.
- [2] V.C. Li, H.-C. Wu, Conditions for pseudo strain-hardening in fiber reinforced brittle matrix composites, *Appl. Mech. Rev.* 45 (1992) 390–398.
- [3] V.C. Li, Engineered cementitious composites—tailored composites through micro-mechanical modeling, in: A.B.N. Banthia, A.A. Mufti (Eds.), *Fiber Reinforced Concrete: Present and the Future* Canadian Society for Civil Engineering, 1998, pp. 74–97 (Montreal).
- [4] V.C. Li, On engineered cementitious composites (ECC), *J. Adv. Concr. Technol.* 1 (2003) 215–230.
- [5] J. Zhang, C.K. Leung, Y. Gao, Simulation of crack propagation of fiber reinforced cementitious composite under direct tension, *Eng. Fract. Mech.* 78 (2011) 2439–2454.
- [6] S. Fan, M. Li, X-ray computed microtomography of three-dimensional microcracks and self-healing in engineered cementitious composites, *Smart Mater. Struct.* 24 (2014) 015021.
- [7] D. Hou, H. Ma, Y. Zhu, Z. Li, Calcium silicate hydrate from dry to saturated state: structure, dynamics and mechanical properties, *Acta Mater.* 67 (2014) 81–94.
- [8] C. Wagner, A. Dollase, V. Slowi, Evaluation of crack patterns in SHCC with respect to water permeability and capillary suction, in: A.e. al (Ed.), *Concrete Repair, Rehabilitation and Retrofitting III*, 2012.
- [9] H. Liu, Q. Zhang, C. Gu, H. Su, V.C. Li, Influence of micro-cracking on the permeability of engineered cementitious composites, *Cem. Concr. Compos.* 72 (2016) 104–113.
- [10] Z. Lu, D. Hou, L. Meng, G. Sun, C. Lu, Z. Li, Mechanism of cement paste reinforced by graphene oxide/carbon nanotubes composites with enhanced mechanical properties, *RSC Adv.* 5 (2015) 100598–100605.
- [11] K. Rokugo, T. Kanda, H. Yokota, N. Sakata, Applications and recommendations of high performance fiber reinforced cement composites with multiple fine cracking (HPRCC) in Japan, *Mater. Struct.* 42 (2009) 1197.
- [12] M.D. Lepech, V.C. Li, Application of ECC for bridge deck link slabs, *Mater. Struct.* 42 (2009) 1185.
- [13] V.C. Li, S. Wang, Flexural behaviors of glass fiber-reinforced polymer (GFRP) reinforced engineered cementitious composite beams, *Dent. Mater. J.* 99 (2002) 11–21.
- [14] G. Fischer, V.C. Li, Effect of matrix ductility on deformation behavior of steel-reinforced ECC flexural members under reversed cyclic loading conditions, *Struct. J.* 99 (2002) 781–790.
- [15] K.E. Kesner, S.L. Billington, Experimental response of precast infill panel connections and panels made with DFRCC, *J. Adv. Concr. Technol.* 1 (2003) 327–333.
- [16] G. Parra-Montesinos, J.K. Wight, Seismic response of exterior RC column-to-steel beam connections, *J. Struct. Eng.* 126 (2000) 1113–1121.
- [17] H.-C. Wu, V.C. Li, Stochastic process of multiple cracking in discontinuous random fiber reinforced brittle matrix composites, *Int. J. Damage Mech.* 4 (1995) 83–102.
- [18] H. Ma, S. Tang, Z. Li, New pore structure assessment methods for cement paste, *J. Mater. Civ. Eng.* 27 (2013) A4014002.
- [19] H. Ma, Mercury intrusion porosimetry in concrete technology: tips in measurement, pore structure parameter acquisition and application, *J. Porous. Mater.* 21 (2014) 207–215.
- [20] K. Tosun-Felekoğlu, B. Felekoğlu, R. Ranade, B.Y. Lee, V.C. Li, The role of flaw size and fiber distribution on tensile ductility of PVA-ECC, *Compos. Part B* 56 (2014) 536–545.
- [21] B.P. Flannery, H.W. Deckman, W.G. Roberge, K.L. D'amico, Three-dimensional X-ray microtomography, *Science* 237 (1987) 1439–1444.

- [22] R.A. Brooks, A quantitative theory of the Hounsfield unit and its application to dual energy scanning, *J. Comput. Assist. Tomogr.* 1 (1977) 487–493.
- [23] P.J. Schilling, B.R. Karedla, A.K. Tatiparthi, M.A. Verges, P.D. Herrington, X-ray computed microtomography of internal damage in fiber reinforced polymer matrix composites, *Compos. Sci. Technol.* 65 (2005) 2071–2078.
- [24] X. Huang, R. Ranade, V.C. Li, Feasibility study of developing green ECC using iron ore tailings powder as cement replacement, *J. Mater. Civ. Eng.* 25 (2012) 923–931.
- [25] D. Marshall, B.N. Cox, A.G. Evans, The mechanics of matrix cracking in brittle-matrix fiber composites, *Acta Metall.* 33 (1985) 2013–2021.
- [26] E. Yang, V.C. Li, Numerical study on steady-state cracking of composites, *Compos. Sci. Technol.* 67 (2007) 151–156.
- [27] C. Leung, V. Li, First-cracking strength of short fiber-reinforced ceramics, *Ceramics Engineering Science Proceedings*, 1989, pp. 1164–1178.
- [28] M. Maalej, V.C. Li, T. Hashida, Effect of fiber rupture on tensile properties of short fiber composites, *J. Eng. Mech.* 121 (1995) 903–913.
- [29] T. Kanda, V.C. Li, Effect of fiber strength and fiber-matrix interface on crack bridging in cement composites, *J. Eng. Mech.* 125 (1999) 290–299.
- [30] E.-H. Yang, S. Wang, Y. Yang, V.C. Li, Fiber-bridging constitutive law of engineered cementitious composites, *J. Adv. Concr. Technol.* 6 (2008) 181–193.
- [31] T. Kanda, V.C. Li, Multiple cracking sequence and saturation in fiber reinforced cementitious composites, *Concr. Res. Technol.* 9 (1998) 19–33.